



INNOVATIVE METHODOLOGY | Higher Neural Functions and Behavior

Separation of hemodynamic signals from GCaMP fluorescence measured with wide-field imaging

 M. T. Valley,^{1*} M. G. Moore,^{2*}  J. Zhuang,¹ N. Mesa,¹ D. Castelli,¹ D. Sullivan,¹ M. Reimers,² and J. Waters¹

¹Allen Institute for Brain Science, Seattle, Washington; and ²Neuroscience Program and Institute for Quantitative Health Science and Engineering, Michigan State University, East Lansing, Michigan

Submitted 13 May 2019; accepted in final form 12 November 2019

Valley MT, Moore MG, Zhuang J, Mesa N, Castelli D, Sullivan D, Reimers M, Waters J. Separation of hemodynamic signals from GCaMP fluorescence measured with wide-field imaging. *J Neurophysiol* 123: 356–366, 2020. First published November 20, 2019; doi:10.1152/jn.00304.2019.—Wide-field calcium imaging is often used to measure brain dynamics in behaving mice. With a large field of view and a high sampling rate, wide-field imaging can monitor activity from several distant cortical areas simultaneously, revealing cortical interactions. Interpretation of wide-field images is complicated, however, by the absorption of light by hemoglobin, which can substantially affect the measured fluorescence. One approach to separating hemodynamics and calcium signals is to use multiwavelength backscatter recordings to measure light absorption by hemoglobin. Following this approach, we develop a spatially detailed regression-based method to estimate hemodynamics. This Spatial Model is based on a linear form of the Beer–Lambert relationship but is fit at every pixel in the image and does not rely on the estimation of physical parameters. In awake mice of three transgenic lines, the Spatial Model offers improved separation of hemodynamics and changes in GCaMP fluorescence. The improvement is pronounced near blood vessels and, in contrast with the Beer–Lambert equations, can remove vascular artifacts along the sagittal midline and in general permits more accurate fluorescence-based determination of neuronal activity across the cortex.

NEW & NOTEWORTHY This paper addresses a well-known and strong source of contamination in wide-field calcium-imaging data: hemodynamics. To guide researchers toward the best method to separate calcium signals from hemodynamics, we compare the performance of several methods in three commonly used mouse lines and present a novel regression model that outperforms the other techniques we consider.

animal behavior; calcium imaging; hemodynamics; optical methods; systems neuroscience

INTRODUCTION

Over the last few years, there has been a sharp increase in the number of mouse lines with GCaMP expression throughout much of neocortex (Bethge et al. 2017; Chen et al. 2012; Daigle et al. 2018; Hasan et al. 2004; Madisen et al. 2015; Weksselblatt et al. 2016; Zariwala et al. 2012), offering the

opportunity to image cortical activity with high signal to noise and genetically targeted expression. As a result, there has been a resurgence in the use of wide-field fluorescence calcium imaging to monitor brain dynamics in vivo, especially in the context of mouse behavior (Allen et al. 2017; Makino et al. 2017; Mitra et al. 2018; Mohajerani et al. 2013; Weksselblatt et al. 2016). Wide-field imaging offers a large field of view (>10 mm), enabling simultaneous imaging of almost all of neocortex, can be performed through intact skull (Silasi et al. 2016; White et al. 2011), eliminating invasive craniotomies, and, compared with laser-scanning techniques, can achieve a faster sampling rate and is relatively simple and inexpensive to implement.

Wide-field imaging also presents some challenges. It lacks the optical sectioning of confocal and multiphoton microscopes, with the result that fluorescence is typically an average across cells and cellular compartments. Emission can originate from intrinsic fluorophores such as flavoproteins (Zipfel et al. 2003), and fluorescence excitation and emission can be affected by endogenous absorbers like hemoglobin. The effects of intrinsic fluorophores can be negligible in mice with bright and strongly expressed fluorophores (e.g., Zhuang et al. 2017). In contrast, the absorption of fluorescence by hemoglobin cannot be overcome with strong fluorophore expression due to the multiplicative effect of absorption on fluorescence. Furthermore, hemoglobin is a strong, broad-spectrum absorber across the excitation and emission wavelengths of GCaMP. Hence, changes in hemoglobin absorption greatly complicate interpretation of GCaMP fluorescence measurements, even in mice with strong GCaMP expression.

Hemodynamics encompasses multiple processes, including neurovascular coupling, in which neural and glial activity are accompanied by dilation of blood vessels and changes in blood oxygenation, resulting in changes in the total concentration of hemoglobin and the ratio of oxygenated to deoxygenated hemoglobin (Berwick et al. 2005; Bouchard et al. 2009; Hillman 2014; Hillman et al. 2007; Malonek and Grinvald 1996; O'Herron et al. 2016; Sirotnin et al. 2009; Stefanovic et al. 2008). Contraction of cardiac, pulmonary and postural muscles can also drive changes in total hemoglobin concentration, via changes in intracranial blood pressure (Gisolf et al. 2004; Huo et al. 2015; Winder et al. 2017). Postural and locomotor influences on hemodynamics are common in awake, behaving

* M. T. Valley and M. G. Moore contributed equally to this study.

Address for reprint requests and other correspondence: M. Valley (e-mail: valley@gmail.com).

animals, making the separation of hemodynamics from activity-related changes in cellular calcium concentration a common challenge in studies of sensory-motor processing in behaving mice.

A common method to estimate hemodynamics during a fluorescence measurement is to simultaneously make one or more “backscatter” or diffuse reflectance measurements (Bouchard et al. 2009; Wekselblatt et al. 2016) in which photons illuminating the brain surface undergo multiple scattering events within the tissue, and those that return to the detector indicate the proportion that was absorbed by hemoglobin. Backscatter need not interact with fluorescence measurements, enabling continuous monitoring of hemodynamics during fluorescence imaging. From backscatter measurements, hemoglobin concentrations are often calculated using a modified Beer–Lambert relationship that relates the absorption of light by oxygenated and deoxygenated hemoglobin to the length of the mean scattering path through tissue (Ma et al. 2016a; White et al. 2011). A weakness of this technique is that mean scattering path lengths are difficult to measure empirically, forcing the use of calculated mean path lengths that do not account for local differences in scattering and absorption. Local differences in path length can lead to substantial errors in the estimated effects of hemodynamics on fluorescence measured with indicators such as GCaMP.

Here, we describe and test a spatially detailed regression model that allows for differences in optical properties across the brain without requiring the estimation of scattering path lengths. With this model, we quantify the correction in green fluorescent protein (GFP) reporter mice and apply the regression model to GCaMP mice, finding that the spatially detailed model provides improved separation of hemodynamics from changes in GCaMP fluorescence, particularly in brain areas where the separation is challenging with previous models.

METHODS

Animals and surgical preparation. We used four mouse lines, from crossing three Cre driver lines with two reporter lines. Cre lines were Rorb-IRES-Cre, RRID:IMSR_JAX:023526, Harris et al. (2014); Cux2-CreERT2, RRID:MMRRC_031778-MU, Franco et al. (2012); and Ntsr1-Cre_GN220, RRID:MMRRC_030648-UCD, Gong et al. (2007). Reporter lines were Ai140, RRID:IMSR_JAX:030220, Daigle et al. (2018), and Ai148, RRID:IMSR_JAX:030328, Daigle et al. (2018).

Crosses were made between animals hemizygous for Ai140 or Ai148 and animals that were either hemi- or homozygous for Cre. We refer to these crosses using abbreviations Cux2-Ai140, Rorb-Ai140, Ntsr1-Ai140, and Cux2-Ai148.

For Cux2-CreERT2 animals, tamoxifen was administered via oral gavage (50 mg/mL in corn oil) at 0.2 mg/g body wt for 3–5 days. Mice were used for experiments ≥ 2 wk following induction.

Fast imaging experiments to assess model performance on heart-rate hemodynamics (Supplemental Fig. S3; all supplemental material is available at <https://github.com/MichaelGMoore/MultiChanHemo>) were performed on three 7-wk-old Ai140 mice with expression driven by retro-orbital injection of a virus (AAV-PHP.eB-syn-Cre, 10^{11} genome copies). Animals were used for experiments 3 wk following viral injection.

Wide-field imaging was performed on 7- to 30-wk-old male and female mice through the intact skull using a modification of the method of Silasi et al. (2016). Under isoflurane anesthesia, the skull was exposed and cleared of periosteum, and a #1.5 borosilicate coverslip (cat. no. 72204-01; Electron Microscopy Sciences) was

fixed to the skull surface with a layer of clear Metabond (Sun Medical). A three-dimensionally printed light shield was fixed around the coverslip using additional Metabond, and the outward-facing surfaces were coated with an opaque resin (Lang Dental Jet liquid; MediMark). A custom titanium headpost was fixed posterior to the light shield/coverslip and dorsal to the cerebellum using Metabond.

Animal experiments were performed in accordance with the recommendations in the *Guide for the Care and Use of Laboratory Animals* of the National Institutes of Health. All animals were handled according to approved institutional animal care and use committee protocols at the Allen Institute for Brain Science, protocol numbers 1408, 1705, and 1806.

Image acquisition and initial image processing. Mice were head-restrained and free to run on a 16.5-cm-diameter disk. With exception of experiments with visual stimulation (Figs. 1 and 5), mice were in the dark. During visual stimulation, stimuli were displayed on a 27-in. liquid-crystal display monitor placed 13.5 cm from the right eye and consisted of high-contrast Gabor gratings spanning 20° of the visual field, positioned at the center of the visual field. Images were presented at 0.25 Hz, and averages were made from ≥ 50 stimulus presentations.

Images were produced by a tandem-lens microscope of custom optomechanical design (Supplemental Fig. S7) built around a pair of identical $\times 1.0$ lenses (Leica 10450028). Epifluorescence illumination used a 470-nm light-emitting diode (LED; Thorlabs M470L3) filtered (Semrock FF01-474/27-50) and reflected by a dichroic mirror (Semrock FF495-Di03-50 $\times 70$) through the objective lens. Backscatter illumination in yellow used an LED (Thorlabs M565L3) and a band-pass filter (Semrock F01-578/21), and backscatter illumination in red used an unfiltered LED (Thorlabs 625L3). Yellow and red illumination was focused onto a one-to-seven fan-out fiber bundle (Thorlabs BF72HS01), and the termination of each of the seven fibers was uniformly spaced circumferentially around a custom light shield surrounding the imaging objective with each fiber terminating at 45° incident to the brain surface. Fluorescence emission was separated from the two backscatter wavelengths using a dichroic beamsplitter (Semrock FF560-FDi01-50 $\times 70$) and passed through an emission filter (Semrock FF01-525/45-50) to a camera while backscatter passed through a high-pass filter (Edmund Optics Y-50, 500 nm) to a second camera.

For all experiments except those in Supplemental Fig. S3, image acquisition used two Hamamatsu Flash4.0 V3 sCMOS cameras. One camera used for detection of fluorescence operated with 10-ms rolling shutter exposure (100 Hz), and the second, which detected backscatter, received triggered exposures at 50 Hz. We used four illumination and detection wavelength bands, fluorescence excitation, fluorescence emission, backscatter at ~ 577 nm, and backscatter at ~ 630 nm, and the spectrum of each band was measured with a spectroradiometer (SpectroCAL; Cambridge Research Systems) revealing mean wavelengths of 472, 522, 577, and 630 nm. Backscatter measurements at 577 and at 630 nm were interleaved with a blank frame (for calculation of fluorescence bleed through), and thus the final sample rate for each channel on the backscatter camera was $50/3 \approx 17$ Hz.

For experiments in Supplemental Fig. S3, a single Hamamatsu Flash4.0 V3 camera was triggered at 200 Hz using the middle 512 lines of the sensor, and LED illumination of 477-, 577-, or 630-nm illumination was sequentially timed relative to each camera frame exposure, producing a frame rate of ~ 66 Hz per channel. Emission was filtered using a 500-nm high-pass filter.

Analysis was performed using MATLAB (R2018a; MathWorks) or Python 2.7. Images were spatially downsampled from $2,048 \times 2,048$ to 128×128 pixels by averaging. A camera offset of 100 counts was subtracted, and camera counts were converted to photoelectrons (2.19 counts per photoelectron). Backscatter signals, acquired at 17 Hz, were filtered with a 5-Hz Butterworth low-pass filter to prevent aliasing of the heartbeat and were then upsampled to 100 Hz and spatially and temporally aligned to the 100-Hz fluorescence signal. No

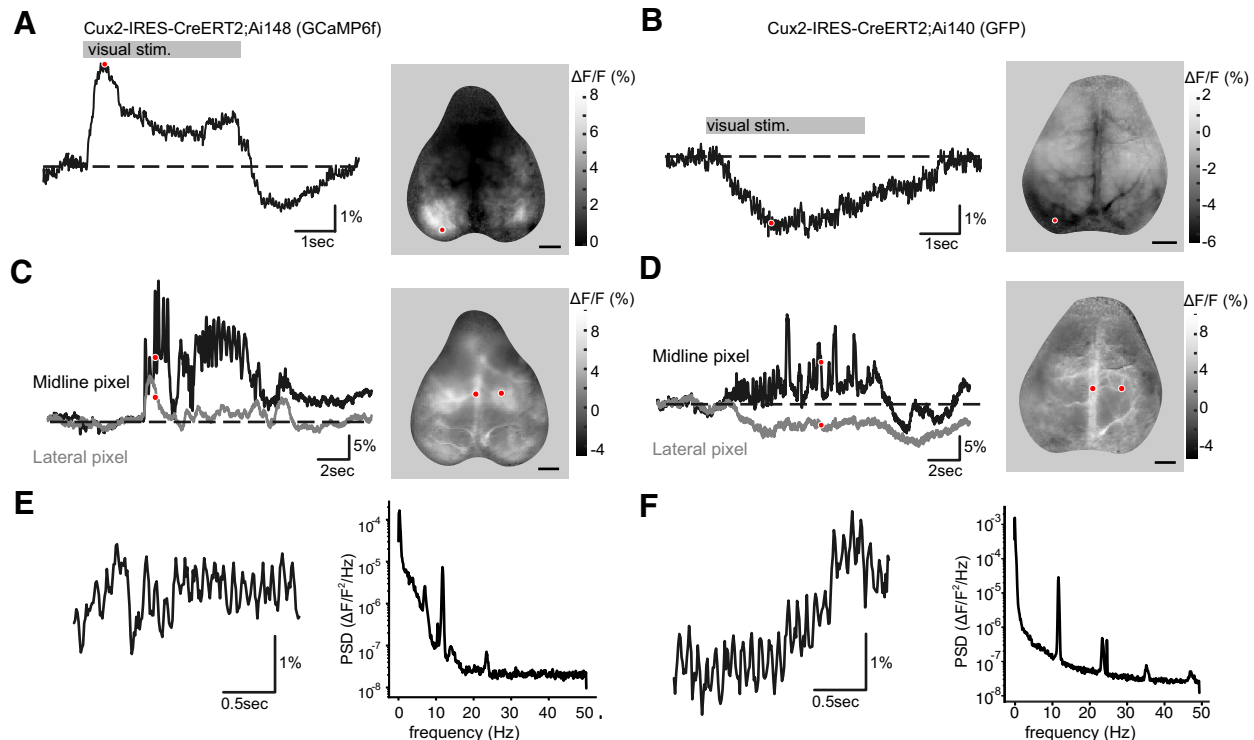


Fig. 1. Hemodynamics in GCaMP and green fluorescent protein (GFP) mice. *A*: fluorescence (F) during a 5-s presentation of a drifting grating. *Left*: fluorescence through time from a pixel in visual cortex (red marker in image). *Right*: image of peak fluorescence at each location. *B*, *left*: time series from a Cux2-Ai140 (GFP) mouse showing mixed GCaMP and hemodynamic responses following the same stimulus (stim.). *Right*: fluorescence in a GFP animal 150–200 ms after stimulation. *C*, *left*: time course of spontaneous activity in a GCaMP6f mouse highlighting 2 pixels on and off the midline vasculature. *Right*: image of the signal from the time indicated (red dots, *left*). *D*: same as *C*, for a GFP mouse. Image scale bars in *A–D* = 2 mm. *E*: example trace (*left*) and power-spectral density (PSD; *right*) of heart-rate oscillations from a GCaMP6f mouse. *F*: example trace (*left*) and power-spectral density (*right*) of heart-rate oscillations from a GFP mouse.

preprocessing, other than spatial downsampling, was applied to the fluorescence image.

Calculation of remaining variance was made with pixelwise normalization to initial variance. To account for its skewness, we took the median of the distribution of remaining variance across pixels to represent the remaining variance in each mouse and averaged across all mice of a genetic background. In GFP mice, the shot noise floor was substantially reduced by the spatial averaging and was 0.5% of the initial variance.

Beer–Lambert model. For Beer–Lambert calculations, we obtained extinction coefficients from tabulated hemoglobin spectra (<https://omlc.org/spectra/hemoglobin/summary.html>) and path lengths from Monte Carlo simulations (Ma et al. 2016a). For each wavelength band, we numerically solved the integral of the path lengths, using the measured spectra of the fluorescence and backscatter wavelength bands (Supplemental Appendix, Eq. 11), and tabulated GFP excitation and emission spectra (<http://www.tsienlab.ucsd.edu/Documents.htm>). The approximations used in what we term the Beer–Lambert and Simplified Beer–Lambert models are described in detail in the Supplemental Appendix.

Regression model. We used 577-nm, 630-nm, or both channels of backscatter data and calculated the weights at each pixel that best fit fluorescence from a GFP-expressing animal using ordinary least squares. When applied to the primary regression problem (estimating fluorescence using 577 + 630-nm backscatter), regularization (L2) had negligible impact on weights or the least-squares error. Generalized cross-validation (using scikit-learn RidgeCV method) predicted a regularization strength parameter (α) < 0.0001 at all pixels in the image.

Alternatively, primary regression weights were estimated using the Spatial Model, which consists of 19×2 secondary weights (Supplemental Table S1) generated by separately fitting 19 statistical projec-

tions of backscatter and fluorescence data (see Supplemental Fig. S6) onto the 577- and 630-nm primary weightings. In our data, Tikhonov (L2) regularization was not used to generate Spatial Model coefficients, but in our code it can optionally be applied, and its strength can be optimized for each Cre line to minimize remaining variance during cross-validation.

A detailed examination of the relationship between the Beer–Lambert and regression models is given in the Supplemental Appendix.

MATLAB code to train and test Spatial Models and perform all variants of regression and Beer–Lambert demixing is available in the online supplement.

RESULTS

Hemodynamics affect fluorescence in GCaMP- and GFP-expressing mice. We used wide-field imaging to monitor fluorescence across neocortex in awake mice expressing GCaMP in neocortical pyramidal neurons. Vasculature was prominent in fluorescence images, and changes in fluorescence near blood vessels were commonplace (Fig. 1). We observed three types of putative hemodynamic effects, defined by their spatial and temporal characteristics. First, we observed stimulus-linked changes in fluorescence that were localized within cortex (Fig. 1A). Fluorescence in visual cortex increased rapidly after the onset of visual stimulation and was followed by a prolonged sag, often to <50% peak amplitude. Following stimulus offset, fluorescence typically decreased below the prestimulus baseline and recovered after ~2 s. The fluorescence increase is a GCaMP-mediated signal. The time course of the sag and

overshoot are consistent with the ~1-s delayed onset and 4- to 5-s decay of local vessel dilation during neurovascular coupling following neural activity (Berwick et al. 2005; Ma et al. 2016b; Maloney and Grinvald 1996; Sirotnin et al. 2009). Second, we observed large amplitude (>10%) fluctuations that were restricted mainly to the midline vasculature (Fig. 1C) and typically included fast transient spikes in fluorescence, sometimes in bouts lasting 1–10 s. These fluctuations may result from changes in venous blood volume along the superior sagittal sinus that relate to movements or postural changes (Gilad et al. 2018; Huo et al. 2015; Qvarlander et al. 2013). Finally, we observed low-amplitude (~1%), global oscillations in the 10- to 14-Hz frequency range of the heart rate (Fig. 1E). As expected, our results suggest that changes in fluorescence measured from GCaMP-expressing mice are a mixture of changes in GCaMP fluorescence and hemodynamics. In many instances, the hemodynamic effects were in the same amplitude range as changes in GCaMP fluorescence.

Consistent with the suggestion that fluorescence in GCaMP animals includes a substantial hemodynamic component, we observed events with similar spatial and temporal characteristics in GFP mice (Fig. 1, B, D, and F), in which fluorescence does not change with intracellular calcium concentration.

Optical strategy for simultaneous measurement of fluorescence and hemodynamics. Hemodynamics alter wide-field fluorescence by absorbing light during excitation or emission (Fig. 2A). Absorption can be measured using backscatter (Fig. 2B). Hemoglobin absorption extends over a broad spectrum that includes wavelengths beyond the excitation and emission bands of GFP and GCaMP, enabling the measurement of hemoglobin concentrations using wavelengths different from those used for fluorescence. Furthermore, oxy- and deoxyhemoglobin absorption spectra differ substantially across the visible spectrum (Fig. 2A), enabling one to distinguish changes in the concentrations of oxy- (HbO) and of deoxyhemoglobin (HbR) using backscatter measurements at two wavelengths with different HbO and HbR absorption, such as 577 and 630 nm (Frostig et al. 1990). We chose these two wavelengths because they are separable from GFP emission and because they sample different parts of the hemoglobin absorption spectra: 577 nm is isosbestic (absorbed equally well by HbO and HbR), whereas 630-nm absorption is heavily weighted toward HbR (see Fig. 2A). Thus the combination of these two wavelengths contains information related to total hemoglobin concentration as well as hemoglobin oxygenation. With the use of two cameras, we simultaneously acquired fluorescence at 100 Hz and two backscatter wavelengths (577 and 630 nm) at ~17 Hz (Fig. 2C). We were unable to adequately sample approximately 8- to 12-Hz heart-rate hemodynamic signals with 17-Hz sampling and used a low-pass filter to remove fluctuations at >5 Hz.

Beer–Lambert model. The Beer–Lambert law has often been employed to estimate light absorption by oxy- and deoxyhemoglobin and thereby separate hemodynamics from changes in indicator fluorescence (Bouchard et al. 2009; Ma et al. 2016a; White et al. 2011). The Beer–Lambert law relates absorption of light to the concentration of the absorbing species, and with the addition of a scattering term it can calculate hemodynamic effects in brain tissue. The basic form of the Beer–Lambert law is $I = I_0 e^{-x(\lambda) \cdot c(t) \cdot \varepsilon(\lambda)}$, where I is the measured light intensity returning from source I_0 , $\varepsilon(\lambda)$ is the wavelength-dependent

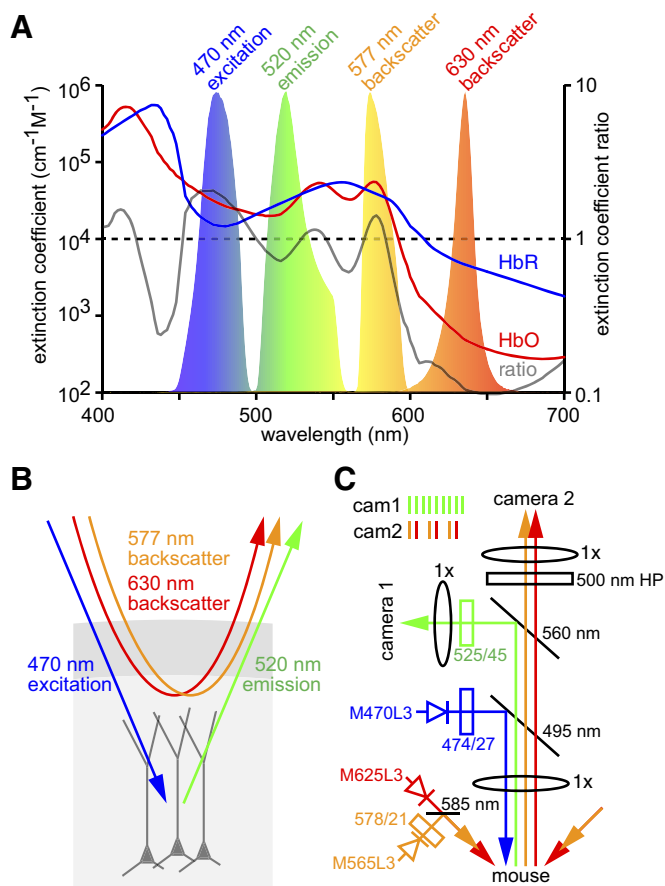


Fig. 2. Simultaneous measurement of GCaMP fluorescence and hemodynamics. **A:** absorption spectra of oxy- and deoxyhemoglobin (HbO and HbR; left axis) in the visible spectrum, the HbO/HbR extinction coefficient ratio (right axis), and normalized spectra of wavebands used in our experiments. **B:** schematic illustration of strategy to estimate absorption of GCaMP excitation and emission (centered at ~470 and ~520 nm, respectively) and of illumination at ~577 and ~630 nm by hemoglobin. Blue illumination is susceptible to absorption when in transit from the light-emitting diode (LED) to the neurons expressing GCaMP. Green fluorescence emission is susceptible to absorption while in transit from GCaMP molecules to the fluorescence camera. Five hundred seventy-seven- and six hundred thirty-nanometer illuminations are susceptible to absorption during entry and during exit from the brain, before and after the scattering events that result in diffuse reflection. **C:** schematic illustration of simultaneous fluorescence and backscatter measurements, with relative locations and wavelength characteristics of LED sources, filters, lenses, dichroic mirrors, and cameras (see Supplemental Fig. S7 for a rendering of the microscope assembly). Camera frame interleaving sequence (inset, top left) shows the continuous acquisition of fluorescence on camera 1 (cam1) and strobing between detection of 577- or 630-nm backscatter and a blank frame on camera 2 (cam2). HP, high pass.

extinction coefficient of the absorbing species, $c(t)$ is the time-varying concentration of the absorbing species, and $x(\lambda)$ is mean path length, the wavelength-dependent distance traveled by scattering light.

We calculated and removed the changes in fluorescence resulting from absorption by oxy- and deoxyhemoglobin, as described previously (Ma et al. 2016a), and quantified the remaining variance. Quantifying performance in a GCaMP mouse is challenging since hemodynamics and changes in indicator fluorescence can each drive changes in measured fluorescence. Consequently, we quantified the performance of hemodynamic correction strategies in GFP-expressing Ai140

mice (Daigle et al. 2018) crossed with three Cre lines, driving GFP expression enriched in different cortical layers: Cux2-Cre (layer 2/3), Rorb-Cre (layer 4), and Ntsr1-Cre (layer 6; Fig. 3C). In these three lines, GFP fluorescence accounts for ~95% of the photons emitted from the preparation (97.9% Cux2-Ai140, 93.7% Rorb-Ai140, and 94.4% Ntsr1-Ai140; Supplemental Fig. S1); thus we expect nearly all changes in fluorescence to result from hemodynamics with a negligible contribution from endogenous fluorophores. Complete separation of hemodynamics from changes in indicator fluorescence would reduce the variance (normalized to initial variance) to ~0.05.

The mean initial variance of the GFP fluorescence (using the median variance of all pixels per mouse) was $5.61 \times 10^{-4}\%$ $\Delta F/F$ in Cux2-Ai140 mice, $7.85 \times 10^{-4}\%$ $\Delta F/F$ in Rorb-Ai140 mice, and $12.52 \times 10^{-3}\%$ $\Delta F/F$ in Ntsr1-Ai140 mice (Fig. 3D). Initial variance was not spatially uniform and was approximately three to five times greater along the midline and over

large vessels than over the center of each hemisphere (Fig. 3A), consistent with a strong influence of movement- or posture-related hemodynamics.

After Beer–Lambert correction, the variance was reduced in all locations across the brain. The median remaining variance across pixels (normalized to initial variance at each pixel), averaged across mice, was 0.19 ± 0.05 in three Cux2-Ai140 mice, 0.14 ± 0.03 in three Rorb-Ai140 mice, and 0.36 ± 0.03 in five Ntsr1-Ai140 mice (Fig. 3E). However, remaining variance differed substantially with location. Normalized remaining variance was generally <0.1 in the center of each hemisphere, over anterior visual cortex, and across much of somatosensory cortex (Fig. 3A). Performance of the correction declined toward the edges of the image, over large vessels, and along the midline, where remaining variance was commonly >0.3 . In these areas, hemodynamic transients remained largely uncorrected, leaving fluorescence from midline cortical regions

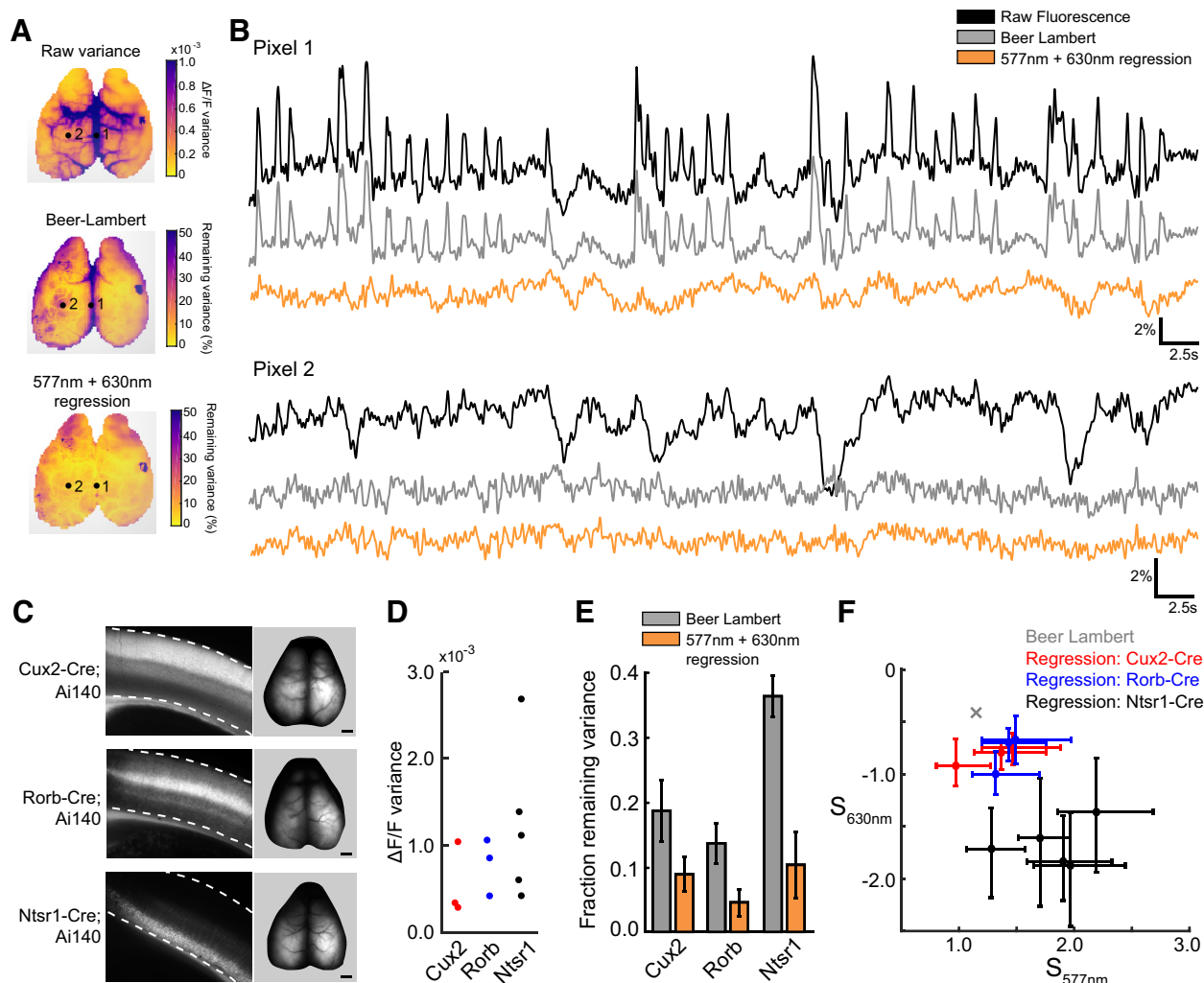


Fig. 3. Comparison of models to explain variance in green fluorescent protein (GFP) mice. **A:** map of variance from a Cux2-Ai140 (GFP) mouse (top) and of remaining variance after correction using 2 models. Numbered dots indicate locations from which traces were extracted for **B**. **B:** example traces of fluorescence (black traces) from 2 example pixels (dots, A) and corrected fluorescence from the Beer–Lambert model (gray traces) and from dual-wavelength linear regression model (yellow traces). **C:** laminar expression patterns in visual cortex of Cux2-Ai140, Rorb-Ai140, and Ntsr1-Ai140 mice. Dashed lines mark the dorsal surface of cortex (top), and the ventral white-matter border of cortex. **D:** initial GFP variance (median variance from all pixels in the brain) for each mouse in the study. **E:** summary of variance remaining after correction (averaged across cortical surface) from three Cre lines. Bars represent means \pm SD. Three Cux2-Ai140 mice, three Rorb-Ai140 mice, and five Ntsr1-Ai140 mice were used. **F:** distribution of regression coefficients (S) for Ai140 mice, fit with 577- and 640-nm backscatter data. With the use of estimated parameters (path length and extinction coefficients), similar but spatially uniform coefficients can be calculated using the Beer–Lambert relationship (gray cross; see Supplemental Appendix for details). Points and error bars represent medians \pm quartiles from all pixels in the image.

such as retrosplenial and cingulate cortex contaminated by hemodynamics.

One common simplification of the Beer–Lambert model is to choose a single extinction coefficient and path length for each wavelength band (rather than integrating over the spectrum of wavelengths; see Supplemental Appendix). When applied to our data, using the extinction coefficients and estimated path lengths of the mean of each wavelength band, average remaining variance was $\geq 40\%$ greater than with the full Beer–Lambert model (remaining variance 0.24 ± 0.03 in 3 Cux2-Ai140 mice, 0.23 ± 0.04 in 3 Rorb-Ai140 mice, and 0.45 ± 0.03 in 5 Ntsr1-Ai140 mice; Supplemental Fig. S5, A and D). Using a single extinction coefficient and path length for each wavelength band substantially impairs performance of the Beer–Lambert model and is best avoided.

Pixelwise regression as an alternative to the Beer–Lambert model. For our Beer–Lambert calculations, we used the same path length estimates at every pixel, a necessary simplification. Naturally, performance of the model is sensitive to the choice of path lengths, particularly the 577-nm path length (Supplemental Fig. S4). We hypothesized that the poor performance of the Beer–Lambert model in some locations results from our inability to account for local variations in optical properties of the tissue, such as mean path length. Consistent with this hypothesis, the two backscatter measurements covaried in midline regions and were typically inversely correlated in other cortical areas (Supplemental Fig. S2), suggesting that a spatially detailed model is needed to most effectively use these two backscatter measurements.

Pixelwise regression using two backscatter measurements is a promising alternative to the Beer–Lambert model because it may account for optical differences across the cortical surface. If done without constraints, the additional spatial degrees of freedom in the regression model should always produce results that are equivalent to or better than the Beer–Lambert model. Conversely, if we assume that path length is the main free parameter in the Beer–Lambert model, and if the true path lengths are identical at all locations in the tissue, then the Beer–Lambert and regression models should converge on the same solution.

We begin by establishing that, in principle, linear regression with two variables can account for hemodynamics independently for each pixel. Measured fluorescence, $I_F(x, y, t)$, can be related to two backscatter intensities, $I_1(x, y, t)$ and $I_2(x, y, t)$, using two assumptions: that the absorbance at each wavelength depends only on two hidden fluctuating variables, $C_{HbO}(x, y, t)$ and $C_{HbR}(x, y, t)$, representing the molar concentrations of oxy- and deoxy-hemoglobin, respectively; and that the absorbance of the fluorescence channel is multiplicative with the true fluorescence, $F(x, y, t)$ (the fluorescence that would be measured in the absence of absorption by hemoglobin). Hence:

$$I_F(x, y, t) = F(x, y, t) T_F [C_{HbO}(x, y, t), C_{HbR}(x, y, t)] I_F^{(ex)}(x, y) \quad (1)$$

$$I_1(x, y, t) = T_1 [C_{HbO}(x, y, t), C_{HbR}(x, y, t)] I_1^{(ex)}(x, y) \quad (2)$$

$$I_2(x, y, t) = T_2 [C_{HbO}(x, y, t), C_{HbR}(x, y, t)] I_2^{(ex)}(x, y), \quad (3)$$

where T_F , T_1 , and T_2 are transmittance functions that depend on HbO and HbR concentrations and $I_F^{(ex)}$, $I_1^{(ex)}$, and $I_2^{(ex)}$ are incident intensities. The dynamic quantities relating to light

intensity and hemoglobin concentration can be expressed in terms of their mean values and deviations:

$$I_\star(x, y, t) = \bar{I}_\star(x, y) + \Delta I_\star(x, y, t) \quad (4)$$

$$F(x, y, t) = \bar{F}(x, y) + \Delta F(x, y, t) \quad (5)$$

$$C_{Hb\star}(x, y, t) = \bar{C}_{Hb\star}(x, y) + \Delta C_{Hb\star}(x, y, t). \quad (6)$$

In our results, the amplitude of the fluorescence signal is large relative to its dynamic range. Under these conditions, Eqs. 1–3 can be linearized in terms of the deviations, permitting elimination of the hemoglobin concentration terms and enabling derivation of the regression problem (see Supplemental Appendix for derivation):

$$\frac{\Delta I_F(x, y, t)}{\bar{I}_F(x, y)} \approx \frac{\Delta F(x, y, t)}{\bar{F}(x, y)} + S_1(x, y) \frac{\Delta I_1(x, y, t)}{\bar{I}_1(x, y)} + S_2(x, y) \frac{\Delta I_2(x, y, t)}{\bar{I}_2(x, y)}. \quad (7)$$

$S_1(x, y)$ and $S_2(x, y)$ are coefficient maps (Fig. 4C). Just as path lengths are the key unknown parameters in the Beer–Lambert model, regression coefficients are the key to separating hemodynamics from changes in indicator fluorescence using the regression model. As a result of the linearization, regression coefficients can be calculated from path lengths (Fig. 3F, and see Supplemental Appendix), although the inverse problem (using regression weights to estimate path length) is underdetermined and cannot be solved without additional constraints.

In GFP mice, where we assume changes in measured fluorescence result from only hemodynamics, $\Delta F(t) \approx 0$, permitting simplification of Eq. 7:

$$\frac{\Delta I_F(x, y, t)}{\bar{I}_F(x, y)} \approx S_1(x, y) \frac{\Delta I_1(x, y, t)}{\bar{I}_1(x, y)} + S_2(x, y) \frac{\Delta I_2(x, y, t)}{\bar{I}_2(x, y)}. \quad (8)$$

From Eq. 8, we can solve for the coefficients (S_1 and S_2) by pixelwise linear regression of $\Delta I_F/\bar{I}_F$ onto $\Delta I_1/\bar{I}_1$ and $\Delta I_2/\bar{I}_2$. The effectiveness of this approach is evaluated via the remaining fluorescence intensity:

$$f(x, y, t) = \frac{\Delta I_F(x, y, t)}{\bar{I}_F(x, y)} - S_1(x, y) \frac{\Delta I_1(x, y, t)}{\bar{I}_1(x, y)} - S_2(x, y) \frac{\Delta I_2(x, y, t)}{\bar{I}_2(x, y)}. \quad (9)$$

$f(x, y, t)$ is expected to approximate $\Delta F(x, y, t)/\bar{F}(x, y)$ so that for GFP mice, $f \approx 0$. Hence, linear regression with two variables can account for fluorescence variance due to hemodynamics independently for each pixel, in the absence of calcium-dependent variance. Changes in the corrected fluorescence decline toward 0 as performance of the regression model approaches the limit of complete separation.

When applied to GFP fluorescence, the regression model improved on the performance of the Beer–Lambert model. The median remaining variance across all pixels, averaged across mice, was 0.08 ± 0.03 in three Cux2-Ai140 mice, 0.05 ± 0.02 in three Rorb-Ai140 mice, and 0.10 ± 0.05 in five Ntsr1-Ai140

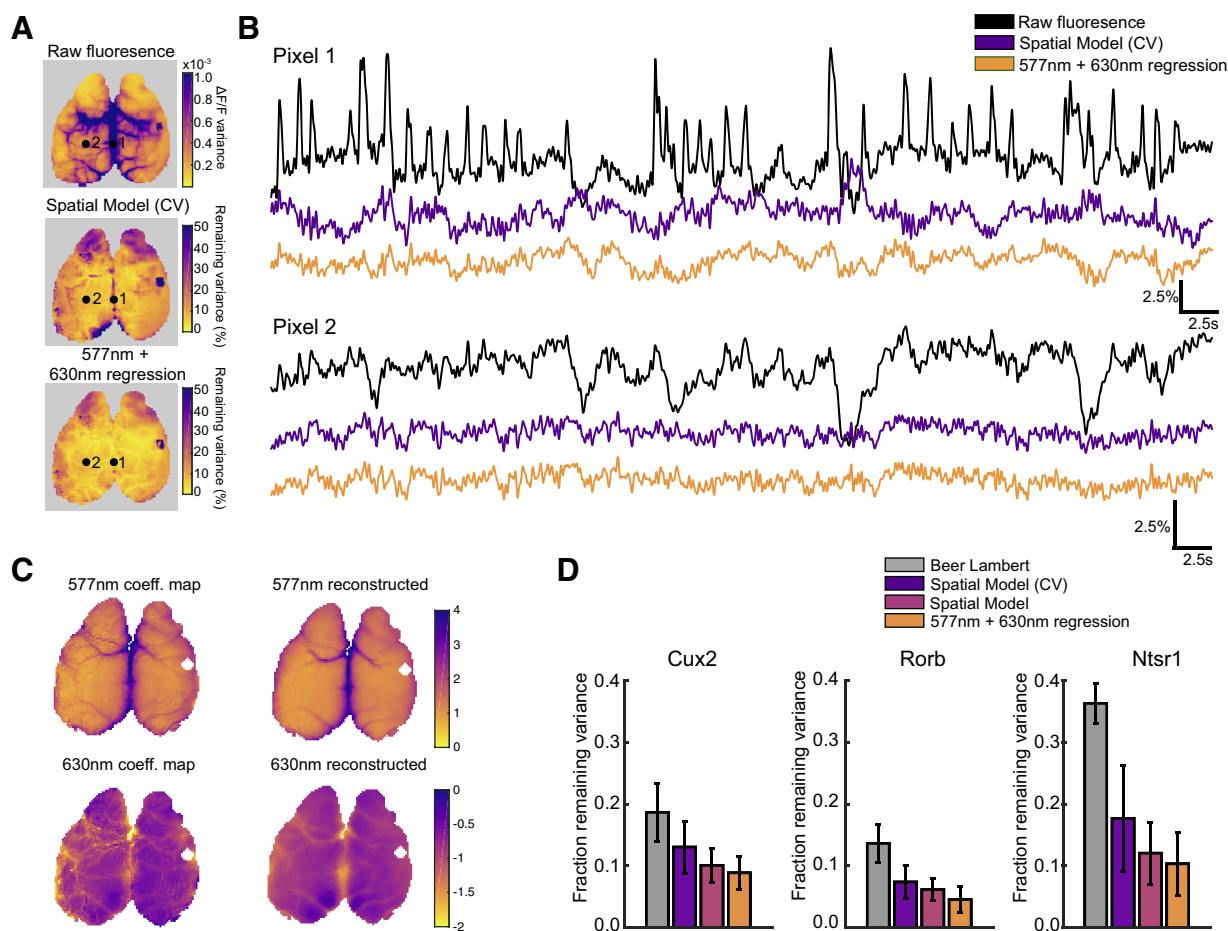


Fig. 4. Evaluation of the Spatial Model. *A*: map of variance from a Cux2-Ai140 (green fluorescent protein, GFP) mouse (*top*) and of remaining variance after correction using the Spatial Model using averaged parameters generated during across-animal leave-1-out cross-validation (Spatial Model CV) and the 2-wavelength regression model. Numbered dots indicate locations from which traces were extracted for *B*. *B*: example traces of fluorescence (black traces) from 2 example pixels (dots, *A*) and of corrected fluorescence from Spatial Model CV and from dual-wavelength linear regression model (yellow traces). *C*, *left*: coefficient (coeff.) maps generated using spatially detailed regression of GFP fluorescence onto 577- and 630-nm backscatter. *Right*: reconstructions of coefficient maps (from held-out data) using the Spatial Model. *D*: comparison of remaining variance across models. Shown are means \pm standard deviation across all animals, where the median remaining variance is taken across all pixels for each animal. F, fluorescence.

mice (Fig. 3*E*), approximately 60–70% reduction in remaining variance relative to the Beer–Lambert model. Regression produced uniformly good correction across most of the brain, with the improved performance being particularly noticeable over large vessels, along the midline, and toward the edges of the brain, where the Beer–Lambert correction was poor (Fig. 3*A*). The large, fast putative movement- or posture-related hemodynamic transients along the midline were largely eliminated by spatially detailed regression (Fig. 3*B*). We conclude that pixelwise regression using two backscatter measurements offers improved separation of hemodynamics from changes in indicator fluorescence, likely because regression enables the model to account for differences in optical properties across the brain.

Interestingly, the mean regression coefficients required for optimal correction differed between mouse lines. Regression coefficients for Cux2-Ai140 and Rorb-Ai140 were clustered (Fig. 3*F*), perhaps because of their common GFP expression in pyramidal apical dendrites that ramify through layers 1–3. Coefficients were noticeably different for Ntsr1-Ai140 mice, with expression in layer 6 pyramidal neurons and dendrites that do not extend beyond layer 4 (Fig. 3*C*). These differences are

consistent with the idea that optical properties such as mean scattering path length differ between mouse lines and must to be adjusted for optimal correction.

The regression model is effective in removing many of the effects of hemodynamics at <5 Hz, but is it equally effective in eliminating heart-rate-related hemodynamics, which occur on a faster time scale? We imaged at higher frame rates using a single camera (~ 66 Hz per channel while multiplexing fluorescence at 520 nm and backscatter at 577 and 630 nm on 1/4 of our camera sensor; Supplemental Fig. S3*A*). Fluorescence traces showed heart-rate oscillations that were corrected by pixelwise regression with the 2 backscatter measurements (Supplemental Fig. S3, *C* and *D*). This alternate experimental approach may be useful for experimentalists who seek a simplified experimental apparatus or for experiments that require faster imaging.

Single-wavelength linear regression. Single-wavelength regression can also be used to separate hemodynamics from changes in indicator fluorescence. Generally, single-wavelength regression employs backscatter at an isosbestic wavelength such as 530 or 577 nm. Consequently, one might expect single-wavelength regression to best account for changes in

total hemoglobin concentration (Frostig et al. 1990) but not changes in blood oxygenation. Again, we used the same data set to compare the performance of single- and two-wavelength regression.

We regressed the 577-nm backscatter measurement against GFP fluorescence, pixelwise:

$$\frac{\Delta I_F(x, y, t)}{\bar{I}_F(x, y)} \approx S_1(x, y) \frac{\Delta I_1(x, y, t)}{\bar{I}_1(x, y)}. \quad (10)$$

The remaining variance after 577-nm single-wavelength regression was 0.15 ± 0.05 in three Cux2-Ai140 mice, 0.09 ± 0.03 in three Rorb-Ai140 mice, and 0.23 ± 0.09 in five Ntsr1-Ai140 mice (Supplemental Fig. S5), approximately two to three times more remaining variance than two-wavelength regression and comparable with the Beer–Lambert model. Unlike the Beer–Lambert model, 577-nm single-wavelength regression performed reasonably well across most pixels (Supplemental Fig. S5A), underlining the importance of allowing for differences in optical properties by tuning the model at each pixel. Overall, the performance of 577-nm single-wavelength regression was intermediate between that of the Beer–Lambert and two-wavelength regression models.

A simplified 577-nm single-wavelength regression model using a coefficient of 1 at all pixels (Xiao et al. 2017) left remaining variance of 0.23 ± 0.06 in three Cux2-Ai140 mice, 0.21 ± 0.03 in three Rorb-Ai140 mice, and 0.43 ± 0.03 in five Ntsr1-Ai140 mice (Supplemental Fig. S5, 577-nm ratiometric demixing). Like other models not tuned pixelwise, correction was particularly poor over large vessels, along the midline, and toward the edges of the hemispheres. However, pixelwise regression is no guarantee of performance: 630-nm single-wavelength pixelwise regression offered poor performance with remaining variance of 0.84 ± 0.10 in three Cux2-Ai140 mice, 0.61 ± 0.04 in three Rorb-Ai140 mice, and 0.68 ± 0.15 in five Ntsr1-Ai140 mice (Supplemental Fig. S5).

Spatial Model to predict regression coefficients in GCaMP mice. Tuning a regression model at each pixel improves performance in many brain areas, but how can we generate pixelwise coefficient maps in GCaMP mice? In GFP mice, we found coefficients by regressing changes in backscatter intensity against changes in fluorescence at each pixel, under the assumption that changes in fluorescence were due to hemodynamics. This assumption is not valid for GCaMP mice because hemodynamics correlate with neuronal activity, so direct regression is not an option. Instead, we developed a Spatial Model that predicts regression coefficients at each pixel using common features of backscatter and fluorescence images that are shared by GFP and GCaMP mice. We trained and validated the performance of this Spatial Model on movies from GFP mice and applied the model to GCaMP mice.

The Spatial Model uses several statistical projections (e.g., stdev, skew, or kurtosis) of backscatter and fluorescence images to predict coefficient maps (Fig. 4C). We regressed primary coefficient maps from GFP animals onto 19 statistical projections (Supplemental Fig. S6) to determine the weighting of features that best predicted the primary regression coefficients (Supplemental Table S1). We tested the performance of the Spatial Model in two stages. First, we trained and tested spatial weights using the same GFP mouse to reveal the performance limit of the Spatial Model. Remaining variance,

averaged across all pixels, was 0.10 ± 0.03 in three Cux2-Ai140 mice, 0.06 ± 0.02 in three Rorb-Ai140 mice, and 0.12 ± 0.05 in five Ntsr1-Ai140 mice (Fig. 4A), close to the performance of the primary regression model. Second, we used leave-one-animal-out cross-validation to generate mean spatial weights for each mouse line (Supplemental Table S1) and applied these mean spatial weights to generate coefficient maps and separate hemodynamics and changes in indicator fluorescence in the left-out (test) mouse. Cross-validation also indicates the expected Spatial Model performance in GCaMP mice. The median remaining variance of all pixels in this second test, averaged across animals, was 0.13 ± 0.04 in three Cux2-Ai140 mice, 0.08 ± 0.03 in three Rorb-Ai140 mice, and 0.21 ± 0.09 in five Ntsr1-Ai140 mice. Hence, in all three mouse lines, the remaining variance was greater than with the two-wavelength regression model (that cannot be directly applied to GCaMP mice) but less than the remaining variance of the Beer–Lambert model. Much of the improvement in performance of the Spatial Model over the Beer–Lambert model is near vessels and along the midline. Hence, we expect the Spatial Model to offer improved separation of hemodynamics and changes in indicator fluorescence versus the Beer–Lambert model when applied to GCaMP mice, particularly for cortical areas along the midline and near large vessels.

Separation of hemodynamics from changes in indicator fluorescence in GCaMP mice. We used the spatially detailed regression model to separate hemodynamics from changes in indicator fluorescence in Cux2-Ai148 mice, with GCaMP6f in superficial pyramidal neurons. We trained the Spatial Model on GFP mice and then applied the resulting coefficient maps to genetically matched GCaMP6 mice (Cux2-Ai140 vs. Cux2-Ai148 mice, etc.). During spontaneous activity, GCaMP variance was sometimes increased and at other times reduced, especially during fast changes in fluorescence during events along the midline (Fig. 5A). During presentation of a visual stimulus, the vasodilatory sag was reduced, in GFP (Fig. 5B) and in GCaMP mice (Fig. 5C), and the baseline overshoot was eliminated. In the GCaMP results, the difference between original and corrected traces was similar in amplitude and time course to the change in measured fluorescence in GFP mice, consistent with successful separation of hemodynamics and changes in indicator fluorescence in GCaMP mice.

DISCUSSION

We quantified the effects of hemodynamics on fluorescence measured from GFP mice with wide-field fluorescence imaging and found that changes in fluorescence can equal or exceed those found in mice that express the calcium-dependent fluorescent indicator GCaMP. As a result, we evaluated the performance of several models in separating hemodynamics from changes in indicator fluorescence, including a new Spatial Model that provided the best demixing performance.

Previous methods have used physical models of light scattering and absorption (Berwick et al. 2005; Devor et al. 2012; Hillman et al. 2007; Malonek and Grinvald 1996), leveraging research on tissue absorbance spectra (Takatani and Graham 1979; Wray et al. 1988), endogenous fluorophores (Zipfel et al. 2003), and models of scattering in tissue (Kohl et al. 2000). Correction strategies based on physical parameters, such as the Beer–Lambert model, may overgeneralize and not account for

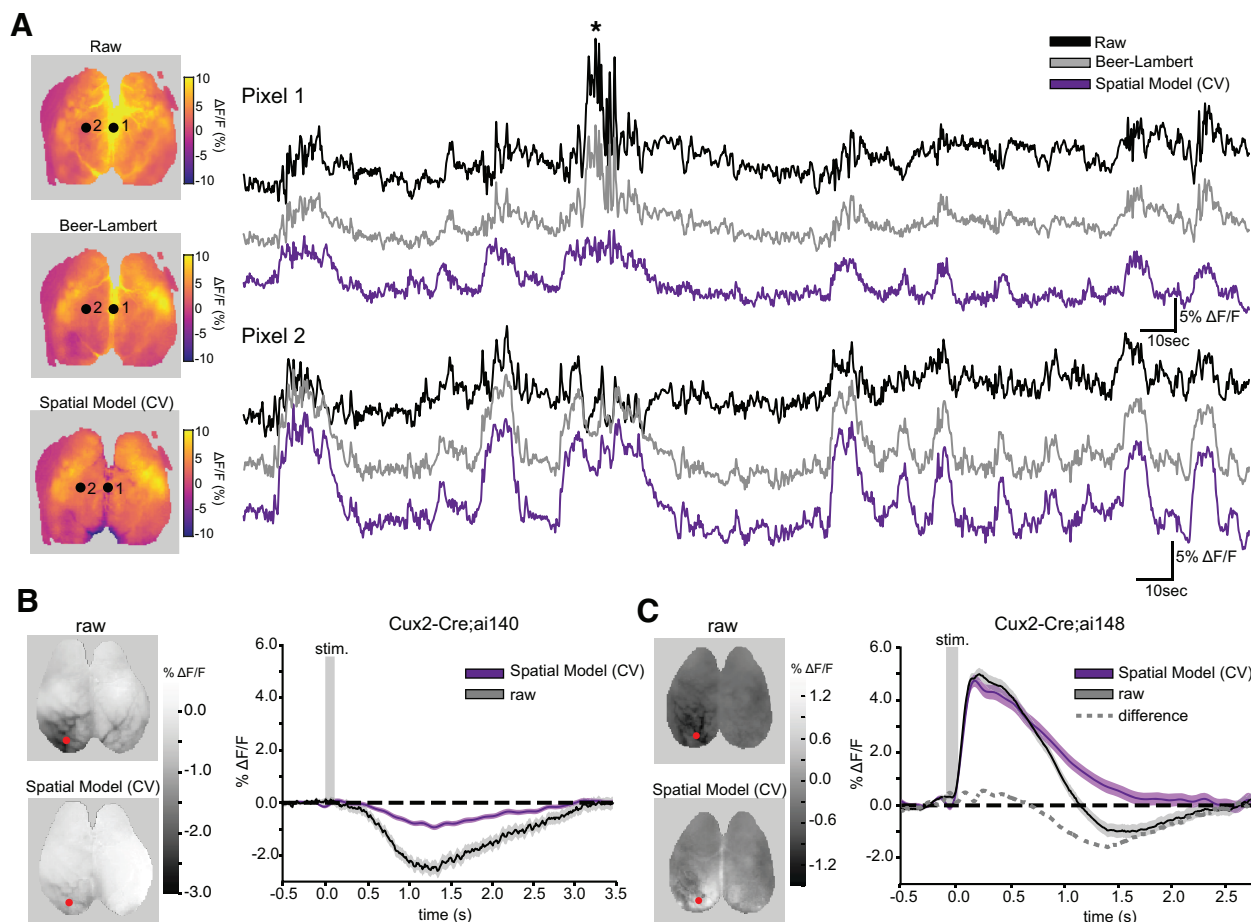


Fig. 5. Demixing hemodynamic responses to a visual stimulus in green fluorescent protein (GFP) and GCaMP mice. **A**: spontaneous activity from a Cux2-Ai148 (GCaMP6f) mouse and correction with Beer–Lambert model and Spatial Model. *Left*: images of fluorescence (F) at a single time point, during midline activity (asterisk, traces). *Right*: $\Delta F/F$ traces for 2 pixels (images, *left*) before (black) and after correction with Beer–Lambert model (gray) and Spatial Model (purple). **B**, *left*: map of mean $\Delta F/F$ 1.5–2 s after stimulus. One hundred-millisecond flashed visual stimulus to the right eye and Cux2-Ai140 (GFP) mouse were used. *Right*: raw trace (black) and trace after Spatial Model correction (purple) extracted from a pixel in V1 (red dot, *left*). **C**, *left*: map of mean $\Delta F/F$ 1.5–2 s after stimulus. One hundred-millisecond flashed visual stimulus to the right eye and Cux2-Ai148 (GCaMP6f) mouse were used. *Right*: raw trace (black) and trace after Spatial Model correction (purple) extracted from a pixel in V1 (red dot, *left*). Shaded regions in **B** and **C** represent SE around the mean ($n > 50$ trials). CV, cross-validation; stim., stimulus.

unique features in cranial windows or tissue heterogeneities such as surface vasculature. One might expect separation models based on physical parameterization to perform poorly in some locations.

Regression models can account for pixelwise differences in optical properties across the cortical surface. We found that the Beer–Lambert model removed most, but not all, hemodynamic effects and poor separation was common near surface blood vessels. In contrast, regression against two backscatter wavelengths outperformed the Beer–Lambert model and performed particularly well near blood vessels. Pixelwise tuning of the model was likely the basis for this outperformance as can be seen from maps of regression coefficients (Fig. 4C), which vary substantially across pixels and highlight vasculature, particularly along the sagittal midline.

Central to our approach is linearization of the Beer–Lambert equation. The resulting linear model cuts through the complexity of trying to estimate the path lengths and extinction coefficients of the Beer–Lambert equation by simplifying the problem to a linear estimation of two variables. Regression against two backscatter wavelengths outperformed other models, eliminating $>90\%$ of variance in most GFP mice. In GFP

mice, using the Spatial Model, residual variance was approximately 0.1–0.2. Hence, correction is not perfect but is close to the expected limit of ~ 0.05 remaining variance after removal of all hemodynamic effects. Residual variance ~ 0.1 above the expected limit corresponds to $\sim 95\%$ reduction in the amplitude of the mean hemodynamic transient ($0.9^{1/2}$), meaning that a large midline hemodynamic artifact that initially caused a 10% change in apparent $\Delta F/F$ in a GFP or GCaMP mouse would be attenuated to $\sim 0.5\%$ $\Delta F/F$ after application of the Spatial Model. The Spatial Model does not completely remove hemodynamic effects from fluorescence traces but typically reduces the amplitudes of apparent changes in fluorescence to close to noise. The performance of single-wavelength regression was similar in some respects to that of the Beer–Lambert model. Both performed adequate correction at many pixels but poorly near blood vessels.

Methods to build statistical maps of backscatter data in the Spatial Model might be improved in several ways. Spatial features could be extracted using deep-learning techniques trained on the primary coefficient maps. Alternatively, simply adding data will add confidence to the Spatial Model's estimate of the primary regression problem, and thus training on more

animals is likely to result in a more robust Spatial Model. It is also possible that nonlinearities, such as fitting time-varying regression coefficients, could form the basis for future improvements in hemodynamic demixing, but the margin for further improvement appears small since the Spatial Model accounts for most hemodynamic effects on fluorescence. Finally, the only hyperparameter in the Spatial Model that can be optimized is the strength of L2 regularization, which in this paper we chose to equal 0 so that the Spatial Model would not penalize fitting infrequent midline transients. In other data, regularization may improve model fit and should be considered by investigators during model training.

An alternative to using backscatter measurements is to stimulate GCaMP with ultraviolet light (~410 nm) where GCaMP fluorescence is not calcium-dependent (Allen et al. 2017). This approach directly measures and corrects for changes in GCaMP emission (but not excitation), presumably caused by hemodynamics. Four hundred ten-nanometer correction can use pixelwise regression of the non-calcium-dependent UV measurement to eliminate hemodynamics from the GCaMP measurement. We found this strategy to be effective over short time periods, but phototoxicity is a concern with prolonged ultraviolet illumination. In addition, the very shallow penetration of 410-nm light (estimated mean scattering path length is ~8 μm) may limit the performance of this approach if applied to fluorescence deep in tissue. Finally, correctly scaling the 410-nm measurement is necessary to avoid removing calcium dynamics that correlate with hemodynamics. We view our Spatial Model as an alternative to this technique for experiments that require nontoxic long-term imaging, although our model is more laborious to construct because it is trained on a separate cohort of GFP animals.

There are several ways to make simultaneous backscatter and fluorescence measurements. Our approach was to use two cameras to maximize fluorescence signal collection. Although this produces excellent signal quality, the microscope and analysis procedures are complicated by the need to compare images from two cameras. Alternatively, we show results using a regression-based correction strategy and temporal multiplexing of both backscatter and fluorescence on a single camera (Supplemental Fig. S3; see also Ma et al. 2016b). This strategy is technically simple and enables the use of a wider range of backscatter wavelengths (including the isosbestic wavelengths around 530 nm); however, at faster frame rates, temporal noise correlations within the sensor may degrade demixing performance (see Supplemental Fig. S3D) and can be avoided with independent cameras.

We propose that experimenters consider different strategies for minimizing the effects of hemodynamics on wide-field fluorescence measurements. The use of longer-wavelength indicators, such as RCaMPs, will reduce the effects of hemodynamics, but GCaMP indicators are in more widespread use. With blue-green indicators, options include the Beer–Lambert model, single-wavelength regression, isosbestic UV illumination, and our Spatial Model. Finding the optimal balance of performance and experimental complexity will depend on several factors, including the proximity of the cortical areas of interest to blood vessels, the extent to which animal behavior and hemodynamic effects on fluorescence are coupled (best measured in GFP mice), the frequency band in which the fluorescence signals of interest occur, and the availability of

transgenic or viral resources to produce matched GFP and GCaMP expression.

ACKNOWLEDGMENTS

We thank Jesse Miles, Bethanny Danskin, and Emily Turschak for technical assistance, and we thank Kevin Takasaki, Nicholas Steinmetz, Elizabeth Hillman, and members of the Allen Institute Neural Coding group for helpful discussions. We thank the Janelia Research Campus for development of GCaMP indicators. We thank the Allen Institute founder, Paul G. Allen, for his vision, encouragement, and support.

Preprint is available at <https://doi.org/10.1101/634923>.

DISCLOSURES

No conflicts of interest, financial or otherwise, are declared by the authors.

AUTHOR CONTRIBUTIONS

M.T.V. and J.W. conceived and designed research; M.T.V., N.M., D.C., and D.S. performed experiments; M.T.V. and M.G.M. analyzed data; M.T.V., M.G.M., J.Z., M.R., and J.W. interpreted results of experiments; M.T.V. prepared figures; M.T.V. and J.W. drafted manuscript; M.T.V., M.G.M., M.R., and J.W. edited and revised manuscript; M.T.V., M.G.M., J.Z., N.M., D.C., D.S., M.R., and J.W. approved final version of manuscript.

REFERENCES

- Allen WE, Kauvar IV, Chen MZ, Richman EB, Yang SJ, Chan K, Gradinaru V, Deverman BE, Luo L, Deisseroth K. Global representations of goal-directed behavior in distinct cell types of mouse neocortex. *Neuron* 94: 891–907.e6, 2017. doi:[10.1016/j.neuron.2017.04.017](https://doi.org/10.1016/j.neuron.2017.04.017).
- Berwick J, Johnston D, Jones M, Martindale J, Redgrave P, McLoughlin N, Schiessl I, Mayhew JE. Neurovascular coupling investigated with two-dimensional optical imaging spectroscopy in rat whisker barrel cortex. *Eur J Neurosci* 22: 1655–1666, 2005. doi:[10.1111/j.1460-9568.2005.04347.x](https://doi.org/10.1111/j.1460-9568.2005.04347.x).
- Bethge P, Carta S, Lorenzo DA, Egolf L, Goniotaki D, Madisen L, Voigt FF, Chen JL, Schneider B, Ohkura M, Nakai J, Zeng H, Aguzzi A, Helmchen F. An R-CaMP1.07 reporter mouse for cell-type-specific expression of a sensitive red fluorescent calcium indicator. *PLoS One* 12: e0179460, 2017. doi:[10.1371/journal.pone.0179460](https://doi.org/10.1371/journal.pone.0179460).
- Bouchard MB, Chen BR, Burgess SA, Hillman EM. Ultra-fast multispectral optical imaging of cortical oxygenation, blood flow, and intracellular calcium dynamics. *Opt Express* 17: 15670–15678, 2009. doi:[10.1364/OE.17.015670](https://doi.org/10.1364/OE.17.015670).
- Chen Q, Cichon J, Wang W, Qiu L, Lee SJ, Campbell NR, Destefino N, Goard MJ, Fu Z, Yasuda R, Looger LL, Arenkiel BR, Gan WB, Feng G. Imaging neural activity using Thy1-GCaMP transgenic mice. *Neuron* 76: 297–308, 2012. doi:[10.1016/j.neuron.2012.07.011](https://doi.org/10.1016/j.neuron.2012.07.011).
- Daigle TL, Madisen L, Hage TA, Valley MT, Knoblich U, Larsen RS, Takeno MM, Huang L, Gu H, Larsen R, Mills M, Bosma-Moody A, Siverts LA, Walker M, Graybuck LT, Yao Z, Fong O, Nguyen TN, Garren E, Lenz GH, Chavarha M, Pendergraft J, Harrington J, Hirokawa KE, Harris JA, Nicovich PR, McGraw MJ, Ollerenshaw DR, Smith KA, Baker CA, Ting JT, Sunkin SM, Lecoq J, Lin MZ, Boyden ES, Murphy GJ, da Costa NM, Waters J, Li L, Tasic B, Zeng H. A suite of transgenic driver and reporter mouse lines with enhanced brain-cell-type targeting and functionality. *Cell* 174: 465–480.e22, 2018. doi:[10.1016/j.cell.2018.06.035](https://doi.org/10.1016/j.cell.2018.06.035).
- Devor A, Sakadžić S, Srinivasan VJ, Yaseen MA, Nizar K, Saisan PA, Tian P, Dale AM, Vinogradov SA, Franceschini MA, Boas DA. Frontiers in optical imaging of cerebral blood flow and metabolism. *J Cereb Blood Flow Metab* 32: 1259–1276, 2012. doi:[10.1038/jcbfm.2011.195](https://doi.org/10.1038/jcbfm.2011.195).
- Franco SJ, Gil-Sanz C, Martinez-Garay I, Espinosa A, Harkins-Perry SR, Ramos C, Müller U. Fate-restricted neural progenitors in the mammalian cerebral cortex. *Science* 337: 746–749, 2012. doi:[10.1126/science.1223616](https://doi.org/10.1126/science.1223616).
- Frostig RD, Lieke EE, Ts'o DY, Grinvald A. Cortical functional architecture and local coupling between neuronal activity and the microcirculation revealed by in vivo high-resolution optical imaging of intrinsic signals. *Proc Natl Acad Sci USA* 87: 6082–6086, 1990. doi:[10.1073/pnas.87.16.6082](https://doi.org/10.1073/pnas.87.16.6082).

- Gilad A, Gallero-Salas Y, Groos D, Helmchen F. Behavioral strategy determines frontal or posterior location of short-term memory in neocortex. *Neuron* 99: 814–828.e7, 2018. doi:10.1016/j.neuron.2018.07.029.
- Gisolf J, van Lieshout JJ, van Heusden K, Pott F, Stok WJ, Karemaker JM. Human cerebral venous outflow pathway depends on posture and central venous pressure. *J Physiol* 560: 317–327, 2004. doi:10.1113/jphysiol.2004.070409.
- Gong S, Doughty M, Harbaugh CR, Cummins A, Hatten ME, Heintz N, Gerfen CR. Targeting Cre recombinase to specific neuron populations with bacterial artificial chromosome constructs. *J Neurosci* 27: 9817–9823, 2007. doi:10.1523/JNEUROSCI.2707-07.2007.
- Harris JA, Hirokawa KE, Sorensen SA, Gu H, Mills M, Ng LL, Bohn P, Mortrud M, Ouellette B, Kidney J, Smith KA, Dang C, Sunkin S, Bernard A, Oh SW, Madisen L, Zeng H. Anatomical characterization of Cre driver mice for neural circuit mapping and manipulation. *Front Neural Circuits* 8: 76, 2014. doi:10.3389/fncir.2014.00076.
- Hasan MT, Friedrich RW, Euler T, Larkum ME, Giese G, Both M, Duebel J, Waters J, Bujard H, Griesbeck O, Tsien RY, Nagai T, Miyawaki A, Denk W. Functional fluorescent Ca²⁺ indicator proteins in transgenic mice under TET control. *PLoS Biol* 2: e163, 2004. doi:10.1371/journal.pbio.0020163.
- Hillman EM. Coupling mechanism and significance of the BOLD signal: a status report. *Annu Rev Neurosci* 37: 161–181, 2014. doi:10.1146/annurev-neuro-071013-014111.
- Hillman EM, Devor A, Bouchard MB, Dunn AK, Krauss GW, Skoch J, Bacskaï BJ, Dale AM, Boas DA. Depth-resolved optical imaging and microscopy of vascular compartment dynamics during somatosensory stimulation. *Neuroimage* 35: 89–104, 2007. doi:10.1016/j.neuroimage.2006.11.032.
- Huo BX, Gao YR, Drew PJ. Quantitative separation of arterial and venous cerebral blood volume increases during voluntary locomotion. *Neuroimage* 105: 369–379, 2015. doi:10.1016/j.neuroimage.2014.10.030.
- Kohl M, Lindauer U, Roß G, Kühl M, Gold L, Villringer A, Dirnagl U. Physical model for the spectroscopic analysis of cortical intrinsic optical signals. *Phys Med Biol* 45: 3749–3764, 2000. doi:10.1088/0031-9155/45/12/317.
- Ma Y, Shaik MA, Kim SH, Kozberg MG, Thibodeaux DN, Zhao HT, Yu H, Hillman EM. Wide-field optical mapping of neural activity and brain hemodynamics: considerations and novel approaches. *Philos Trans R Soc Lond B Biol Sci* 371: 20150360, 2016a. [Erratum in *Philos Trans R Soc Lond B Biol Sci* 372: 20160539, 2017.] doi:10.1098/rstb.2015.0360.
- Ma Y, Shaik MA, Kozberg MG, Kim SH, Portes JP, Timmerman D, Hillman EM. Resting-state hemodynamics are spatiotemporally coupled to synchronized and symmetric neural activity in excitatory neurons. *Proc Natl Acad Sci USA* 113: E8463–E8471, 2016b. doi:10.1073/pnas.1525369113.
- Madisen L, Garner AR, Shimaoka D, Chuong AS, Klapoetke NC, Li L, van der Bourg A, Niino Y, Ego L, Monetti C, Gu H, Mills M, Cheng A, Tasic B, Nguyen TN, Sunkin SM, Benucci A, Nagy A, Miyawaki A, Helmchen F, Empson RM, Knöpfel T, Boyden ES, Reid RC, Carandini M, Zeng H. Transgenic mice for intersectional targeting of neural sensors and effectors with high specificity and performance. *Neuron* 85: 942–958, 2015. doi:10.1016/j.neuron.2015.02.022.
- Makino H, Ren C, Liu H, Kim AN, Kondapaneni N, Liu X, Kuzum D, Komiyama T. Transformation of cortex-wide emergent properties during motor learning. *Neuron* 94: 880–890.e8, 2017. doi:10.1016/j.neuron.2017.04.015.
- Malonek D, Grinvald A. Interactions between electrical activity and cortical microcirculation revealed by imaging spectroscopy: implications for functional brain mapping. *Science* 272: 551–554, 1996. doi:10.1126/science.272.5261.551.
- Mitra A, Kraft A, Wright P, Acland B, Snyder AZ, Rosenthal Z, Czerniewski L, Bauer A, Snyder L, Culver J, Lee JM, Raichle ME. Spontaneous infra-slow brain activity has unique spatiotemporal dynamics and laminar structure. *Neuron* 98: 297–305.e6, 2018. doi:10.1016/j.neuron.2018.03.015.
- Mohajerani MH, Chan AW, Mohsenvand M, LeDue J, Liu R, McVea DA, Boyd JD, Wang YT, Reimers M, Murphy TH. Spontaneous cortical activity alternates between motifs defined by regional axonal projections. *Nat Neurosci* 16: 1426–1435, 2013. doi:10.1038/nn.3499.
- O'Herron P, Chhatbar PY, Levy M, Shen Z, Schramm AE, Lu Z, Kara P. Neural correlates of single-vessel haemodynamic responses in vivo. *Nature* 534: 378–382, 2016. doi:10.1038/nature17965.
- Qvarlander S, Sundström N, Malm J, Eklund A. Postural effects on intracranial pressure: modeling and clinical evaluation. *J Appl Physiol* (1985) 115: 1474–1480, 2013. doi:10.1152/japplphysiol.00711.2013.
- Silasi G, Xiao D, Vanni MP, Chen AC, Murphy TH. Intact skull chronic windows for mesoscopic wide-field imaging in awake mice. *J Neurosci Methods* 267: 141–149, 2016. doi:10.1016/j.jneumeth.2016.04.012.
- Sirotnin YB, Hillman EM, Bordier C, Das A. Spatiotemporal precision and hemodynamic mechanism of optical point spreads in alert primates. *Proc Natl Acad Sci USA* 106: 18390–18395, 2009. doi:10.1073/pnas.0905509106.
- Stefanovic B, Hutchinson E, Yakovleva V, Schram V, Russell JT, Belluscio L, Koretsky AP, Silva AC. Functional reactivity of cerebral capillaries. *J Cereb Blood Flow Metab* 28: 961–972, 2008. doi:10.1038/sj.jcbfm.9600590.
- Takalani S, Graham MD. Theoretical analysis of diffuse reflectance from a two-layer tissue model. *IEEE Trans Biomed Eng* 26: 656–664, 1979. doi:10.1109/TBME.1979.326455.
- Wekselblatt JB, Flister ED, Piscopo DM, Niell CM. Large-scale imaging of cortical dynamics during sensory perception and behavior. *J Neurophysiol* 115: 2852–2866, 2016. doi:10.1152/jn.01056.2015.
- White BR, Bauer AQ, Snyder AZ, Schlaggar BL, Lee JM, Culver JP. Imaging of functional connectivity in the mouse brain. *PLoS One* 6: e16322, 2011. doi:10.1371/journal.pone.0016322.
- Winder AT, Echagarruga C, Zhang Q, Drew PJ. Weak correlations between hemodynamic signals and ongoing neural activity during the resting state. *Nat Neurosci* 20: 1761–1769, 2017. doi:10.1038/s41593-017-0007-y.
- Wray S, Cope M, Delpy DT, Wyatt JS, Reynolds EO. Characterization of the near infrared absorption spectra of cytochrome *aa₃* and haemoglobin for the non-invasive monitoring of cerebral oxygenation. *Biochim Biophys Acta* 933: 184–192, 1988. doi:10.1016/0005-2728(88)90069-2.
- Xiao D, Vanni MP, Mitelut CC, Chan AW, LeDue JM, Xie Y, Chen AC, Swindale NV, Murphy TH. Mapping cortical mesoscopic networks of single spiking cortical or sub-cortical neurons. *eLife* 6: e19976, 2017. doi:10.7554/eLife.19976.
- Zariwala HA, Borghuis BG, Hoogland TM, Madisen L, Tian L, De Zeeuw CI, Zeng H, Looger LL, Svoboda K, Chen TW. A Cre-dependent GCaMP3 reporter mouse for neuronal imaging in vivo. *J Neurosci* 32: 3131–3141, 2012. doi:10.1523/JNEUROSCI.4469-11.2012.
- Zhuang J, Ng L, Williams D, Valley M, Li Y, Garrett M, Waters J. An extended retinotopic map of mouse cortex. *eLife* 6: e18372, 2017. doi:10.7554/eLife.18372.
- Zipfel WR, Williams RM, Christie R, Nikitin AY, Hyman BT, Webb WW. Live tissue intrinsic emission microscopy using multiphoton-excited native fluorescence and second harmonic generation. *Proc Natl Acad Sci USA* 100: 7075–7080, 2003. doi:10.1073/pnas.0832308100.